

Review of Control Techniques for Dual Three-phase PMSM Drives with Low Carrier Ratios

Minrui Gu, Zheng Wang, *Senior Member, IEEE*, Ming Cheng, *Fellow, IEEE*,
Weifeng Su, Linyue Shang, and Po Liu

Abstract—The dual three-phase PMSM (DTP-PMSM) drives have received wide attention at high-power high-efficiency applications due to their merits of high output current ability and copper-loss-free field excitation. Meanwhile, the DTP-PMSM drive provides higher fault-tolerant capability for high-reliability applications, e.g., pumps and actuators in aircraft. For high-power drives with limited switching frequencies and high-speed drives with large fundamental frequencies, the ratio of switching frequency to fundamental frequency, i.e., the carrier ratio, is usually below 15, which would significantly degrade the control performance. The purpose of this paper is to review the recent work on the modulation and control schemes for improving the operation performance of DTP-PMSM drives with low carrier ratios. Specifically, three categories of methods, i.e., the space vector modulation based control, the model predictive control (MPC), and the optimized pulse pattern (OPP) based control are reviewed with principles and performance. In addition, brief discussions regarding the comparison and future trends are presented for low-carrier-ratio (LCR) modulation and control schemes of DTP-PMSM drives.

Index Terms—Dual three-phase permanent magnet synchronous motor (DTP-PMSM), Low-carrier-ratio (LCR), Complex vector control, Model predictive control (MPC), Optimized pulse pattern (OPP).

I. INTRODUCTION

THE dual three-phase permanent magnet (PM) synchronous motor (DTP-PMSM) drive is an attractive solution for high-power and high-reliability applications such as ship propulsion, wind power generation, shale gas extraction, actuators in aircraft due to their advantages of lower current stress and higher fault tolerant capability [1]. Fig. 1 shows a typical configuration of two-level inverter fed DTP-PMSM drives. It can be observed that there is a 30-

degree spatial shift between the two sets of three-phase windings to eliminate the sixth-order torque pulsation [2]. The neutral points of the two sets of three-phase windings are typically isolated to eliminate zero-sequence components in stator currents. The fault-tolerant capability of DTP-PMSM can be further enhanced with connected neutrals. However, it requires additional control of zero-sequence current, which may increase complexity of control of DTP-PMSM. Therefore, the low-carrier-ratio (LCR) control techniques are investigated for DTP-PMSM with isolated neutrals in this paper. It is noted that the design principles are also suitable for the drives with connected neutrals by considering control of zero-sequence current components.

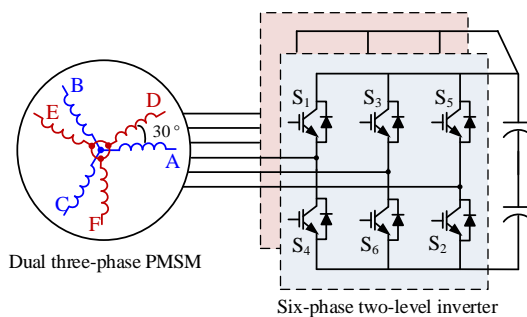


Fig. 1. Configuration of two-level inverter-fed DTP-PMSM drives.

The switching frequency of switching devices is strictly limited at high-power applications due to the stress on heat dissipation [3]-[4]. Meanwhile, high-speed motor drives are usually with high fundamental frequencies [5]-[6]. Consequently, the ratio of switching frequency to the fundamental frequency, called the carrier ratio, is low for both high-power motor drives and high-speed motor drives [7]-[8]. The typical value is below 15. The LCR operating condition not only leads to the increment in stator current harmonics and torque pulsation but also causes significant control delay and distinct coupling effects. For three-phase motor drives, the modulation and control schemes have been intensively investigated for the LCR operation, which can be divided into three categories as shown in Fig. 2. The first category is to improve the performance of space vector pulse width modulation (SVPWM) based vector control schemes. The discretization characteristic and signal delay effect are carefully considered while modeling and controlling PMSM to suppress current harmonics. The improved modulation strategy includes multisampling space vector modulation (MS-SVM) [9]-[12] and natural sampling based space vector modulation

Manuscript received December 04, 2024; revised March 21, 2025; accepted April 14, 2025. Date of publication June 25, 2025; Date of current version May 16, 2025.

This work was supported by the National Key Research and Development Program of China under the grant of 2022YFB3403100. (Corresponding author: Zheng Wang)

Minrui Gu, Zheng Wang, and Ming Cheng are with the School of Electrical Engineering, Southeast University, Nanjing 210096, China (e-mail: 230228726@seu.edu.cn; zwang@eee.hku.hk; mcheng@seu.edu.cn).

Weifeng Su is with China TX IIoT Co., Ltd., Beijing, China (e-mail: wfsu@163.com).

Linyue Shang is with CRRC Xi'an Yonge Electric Intelligent Drive Co., Ltd., Xi'an, China (e-mail: 89292033@qq.com).

Po Liu is with CRRC Yongji Electric Co., Ltd., Xi'an, China (e-mail: 18635985806@163.com).

Digital Object Identifier 10.30941/CESTEMS.2025.00016

(NS-SVM) [13]-[15]. The control scheme includes complex vector control [16]-[23] and deadbeat control [24]-[26]. For time being, other control methods such as sliding mode control and active disturbance rejection control (ADRC) are usually used together with SVM strategy. Their harmonic and torque performance with LCR operation are similar to those of the first category of method mentioned in this paper. The second category is to employ multistep finite control set (FCS) model predictive control (MPC) schemes including trajectory extrapolated algorithm [27]-[30] and sphere decoding method [31]-[33]. High sampling frequency is configured to figure out the optimal space vector discretely. The main concern is to increase the prediction horizon for performance improvement on the premise of a reasonable computational burden. The third category is the optimized pulse pattern (OPP) based methods to improve steady-state and dynamic performance simultaneously [34]-[41]. The pulse pattern is optimized offline to ensure steady-state performance, while the control schemes such as flux trajectory tracking control are used for improving the dynamic performance.

However, all the LCR modulation and control schemes mentioned above are focused on three-phase motor drives. The main difference between three-phase PMSM and DTP-PMSM lies in that the control dimension is increased and the additional coupling factor could lead to smaller impedance of harmonic subspaces, which further increases the difficulty in handling at LCR operating conditions. Moreover, the trade-off optimization is required for mitigations of torque ripple and stator current harmonics since the torque ripple is mainly determined by current components in the torque subspace while harmonics in both torque and harmonic subspaces contribute to stator current harmonics of DTP-PMSM. Compared to three-phase PMSM motor drives, the research on LCR modulation and control of DTP-PMSM drives is less. The purpose of this paper is to present a technical review and investigation of recent work on modulation and control strategies of DTP-PMSM drives with low carrier ratios. In Sections II to IV, three categories, i.e., PWM based methods, FCS based methods and OPP based methods for DTP-PMSM drives with low carrier ratios are reviewed respectively. Then, different kinds of methods are compared and future trends of the techniques are prospected in Section V. Finally, conclusions are drawn in Section VI.

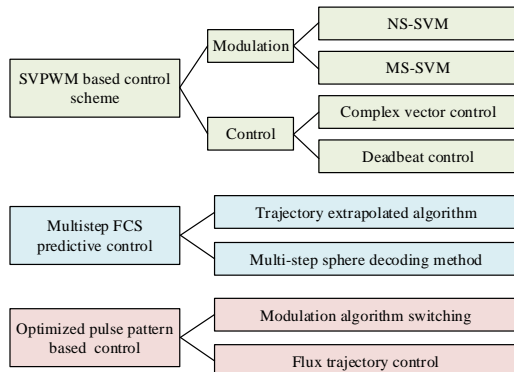


Fig. 2. Classification of research of control for three-phase drives with low carrier ratios.

II. CARRIER PWM BASED CONTROL METHODS

A. Carrier PWM Based LCR Techniques for Three-phase Motor Drives

The natural sampling PWM (NS-PWM) is regarded to provide superior harmonic performance and lower control delay than other carrier-based PWM schemes. However, the requirement of analog implementation limits the application of NS-PWM with digital implementation. Fig. 3 shows the principle of different modulation strategies approximating NS-PWM, which are called MS-SVM and NS-SVM [42]. As shown in the blue curve in Fig. 3(a), MS-SVM increases the sampling frequency and the dwell time is updated within each sampling cycle to approach NS-PWM. Defining N_{stc} as the ratio of sampling frequency to carrier frequency, it is revealed in [11]-[12] that the control delay of MS-SVM is $1.5T_c/N_{stc}$. T_c is the carrier period. On the other hand, as shown in the brown line in Fig. 3(b), intersections of the continuous dwell time equations and the carrier equation are directly calculated in NS-SVM, with the sampling frequency unchanged [13]-[15]. The main difference is that the digital delay in MS-SVM is smaller than that in NS-SVM, therefore enabling higher control bandwidth.

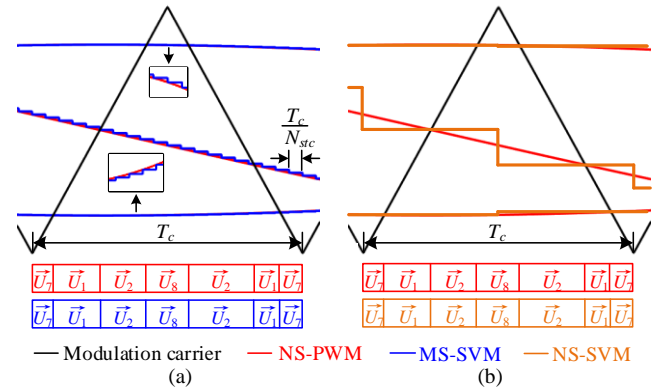


Fig. 3. Comparison of different modulations [42]. (a) MS-SVM. (b) NS-SVM.

From the perspective of control, the main efforts have been devoted to the accurate modeling of drive systems at LCR operating conditions. The digital delay causes significant coupling between dq-axis currents of the motor and influences the system stability. At an early stage, the amplitude and phase compensation is conducted between the reference voltage and the actual stator voltage based on the voltage-second balance principle. Further, complex vector modeling of PMSM is reported [16]-[22], where models are established in both continuous and discrete domains. Different discrete LCR controllers have been compared in [23]. Except for the controller designed in the frequency domain, the deadbeat control also receives attention for the LCR control [24]-[26]. The theoretical performance of deadbeat control could be better but the parameter sensitivity requires careful consideration.

B. MS-SVM Based Control for DTP-PMSM Drives

With the vector space decomposition (VSD) approach, the voltage and current space vectors of DTP-PMSM can be

decoupled into three two-dimensional orthogonal subspaces: $\alpha\beta$ -subspace (torque subspace), xy -subspace (harmonic subspace), and o_1o_2 -subspace (zero sequence subspace) [43], where the VSD decomposition matrix T_{VSD} is expressed as:

$$T_{\text{VSD}} = \frac{1}{3} \begin{bmatrix} 1 & -\frac{1}{2} & -\frac{1}{2} & \frac{\sqrt{3}}{2} & -\frac{\sqrt{3}}{2} & 0 \\ 0 & \frac{\sqrt{3}}{2} & -\frac{\sqrt{3}}{2} & \frac{1}{2} & \frac{1}{2} & -1 \\ 1 & -\frac{1}{2} & -\frac{1}{2} & -\frac{\sqrt{3}}{2} & \frac{\sqrt{3}}{2} & 0 \\ 0 & -\frac{\sqrt{3}}{2} & \frac{\sqrt{3}}{2} & \frac{1}{2} & \frac{1}{2} & -1 \\ 1 & 1 & 1 & 0 & 0 & 0 \\ 0 & 0 & 0 & 1 & 1 & 1 \end{bmatrix} \quad (1)$$

The obtained model of DTP-PMSM in the synchronous rotating frame can be expressed as:

$$\begin{cases} u_d = R_s i_d + L_d di_d / dt - \omega L_q i_q \\ u_q = R_s i_q + L_q di_q / dt + \omega L_d i_d + \omega \psi_f \\ u_{z1} = R_s i_{z1} + L_{z1} di_{z1} / dt + \omega L_{z2} i_{z2} \\ u_{z2} = R_s i_{z2} + L_{z2} di_{z2} / dt - \omega L_{z1} i_{z1} \end{cases} \quad (2)$$

where u_d , u_q , u_{z1} and u_{z2} are the dq-axis and z_1z_2 -axis stator voltages, respectively. i_d , i_q , i_{z1} and i_{z2} are the dq-axis and z_1z_2 -axis stator currents, respectively. R_s is the stator resistance. ω is the fundamental electrical angular frequency. ψ_f denotes the flux linkage produced by the PM. L_d , L_q , L_{z1} and L_{z2} are the dq-axis and z_1z_2 -axis inductances, which can be expressed as:

$$\begin{aligned} L_d &= L_s + (1 + \chi) L_{md}, L_q = L_s + (1 + \chi) L_{mq} \\ L_{z1} &= L_s + (1 - \chi) L_{md}, L_{z2} = L_s + (1 - \chi) L_{mq} \end{aligned} \quad (3)$$

where L_s is the leakage inductance, L_{md} and L_{mq} are the dq-axis main inductances of each set of three-phase windings. The coefficient χ denotes the coupling factor of the two sets of three-phase windings, whose typical value is within the range of 0 to 1. The coefficient χ of the segmentally-designed or concentrated-winding DTP-PMSM is closer to 0, whereas that value of the distributed-winding DTP-PMSM is closer to 1. It can be seen in (2) that current and voltage components in the torque subspace are decoupled from those in the harmonic subspace. Using surface-mounted DTP-PMSM as an example, the model can be simplified as:

$$\begin{cases} u_d = R_s i_d + L_s di_d / dt - \omega L_s i_q \\ u_q = R_s i_q + L_s di_q / dt + \omega L_s i_d + \omega \psi_f \\ u_{z1} = R_s i_{z1} + L_z di_{z1} / dt + \omega L_z i_{z2} \\ u_{z2} = R_s i_{z2} + L_z di_{z2} / dt - \omega L_z i_{z1} \end{cases} \quad (4)$$

where,

$$L_s = L_s + (1 + \chi) L_m, L_z = L_s + (1 - \chi) L_m, L_m = L_{md} = L_{mq} \quad (5)$$

It can be observed in (4) and (5) that the main difference between the DTP-PMSM and three-phase PMSM lies in that the state variable dimension is increased from two to four, where the impedance of the z_1z_2 -subspace might be much smaller than that of the dq-subspace with $\chi=1$. The low-order

harmonic voltages induced by regular sampling in the standard SVM scheme could cause large current harmonics in the harmonic subspaces. Instead, MS-SVM method could improve the harmonic performance by approaching NS-PWM. In comparison, the model of three-phase PMSM is:

$$\begin{cases} u_d = R_s i_d + L_s di_d / dt - \omega L_s i_q \\ u_q = R_s i_q + L_s di_q / dt + \omega L_s i_d + \omega \psi_f \end{cases} \quad (6)$$

It can be observed that the difference between three-phase PMSM and DTP-PMSM is that the two sets of three-phase stator voltage and current in DTP-PMSM are decoupled to the torque subspace and the harmonic subspace with different inductance values. The torque generation is only related to the current components in the torque subspace.

The complex-vector modeling and control method can be applied to surface-mounted DTP-PMSM conveniently. Fig. 4 shows the control scheme of the MS-SVM based complex vector control for DTP-PMSM [42]. The model in dq-subspace can be rewritten as:

$$\mathbf{u}_{dq} = R_s \mathbf{i}_{dq} + L_s d\mathbf{i}_{dq} / dt + j\omega L_s \mathbf{i}_{dq} + j\omega \psi_f \quad (7)$$

where \mathbf{u}_{dq} and \mathbf{i}_{dq} denote the voltage vector and current vector, respectively. $j\omega \psi_f$ can be regarded as a slowly changing disturbance due to the large mechanical inertia. Considering that the control delay of MS-SVM scheme is relatively small, the modeling and controller design are implemented in the continuous domain. The complex vector transfer function $F_{dq}(s)$ from \mathbf{u}_{dq} to \mathbf{i}_{dq} can be expressed as:

$$F_{dq}(s) = \frac{\mathbf{i}_{dq}(s)}{\mathbf{u}_{dq}(s)} = \frac{1}{R_s + sL_s + j\omega L_s} \quad (8)$$

The digital delay can be expressed as:

$$F_{\text{delay}}(s) = \frac{\mathbf{u}_{dq}(s)}{\mathbf{u}_{dq}^*(s)} = e^{-\tau_d s} e^{-j\omega \tau_d} \quad (9)$$

where τ_d denotes the digital delay, and \mathbf{u}_{dq}^* is the reference voltage vector. With (8) and (9), the transfer function $F_{dq}(s)$ from \mathbf{u}_{dq}^* to \mathbf{i}_{dq} can be expressed as:

$$F_{dq}(s) = F_{dq}(s) F_{\text{delay}}(s) = \frac{\mathbf{i}_{dq}(s)}{\mathbf{u}_{dq}^*(s)} = \frac{e^{-\tau_d s} e^{-j\omega \tau_d}}{R_s + sL_s + j\omega L_s} \quad (10)$$

It can be observed that $F_{dq}(s)$ contains the imaginary part, which corresponds to the cross-coupling of dq-axis current control. For standard single sampling SVM scheme, the digital delay τ_d is approximated to $1.5T_c$. With the carrier ratio decreased, $\omega \tau_d$ increases and the imaginary part of $F_{dq}(s)$ increases, leading to the more severe coupling of dq-axis current control. Instead, the delay effect can be neglected due to the small control delay $1.5T_c/N_{\text{stc}}$ in the MS-SVM scheme. Consequently, the controller with MS-SVM can be designed as:

$$F_{rs}(s) = g_c (R_s + sL_s + j\omega L_s) / s \quad (11)$$

where g_c is the controller parameter depending on performance requirements. The final open-loop transfer function $F_o(s)$ is:

method is to evaluate the length within which the switching state can be maintained while tracking errors of all controlled variables are within the allowable range. This length is defined as the extrapolation length. Dividing the extrapolation length by the commutation number required to reach the switching state, it yields the cost function, which indicates the average switching frequency this switching state produces. As shown in Fig. 6, the sampling instant is at kT_s and the loading instant of the selected vector is at $(k+1)T_s$. The values of $i_q(k+1)$ and $i_q(k+2)$ are calculated based on the model of electric machines, whereas the values at other instants are obtained by linear extrapolation. It can be observed that the extrapolation length of i_q for the evaluated switching state is 3 in Fig. 6. Following the same rule, the extrapolation length of other controlled variables can be calculated, and the smallest value is the final extrapolation length of the evaluated switching state.

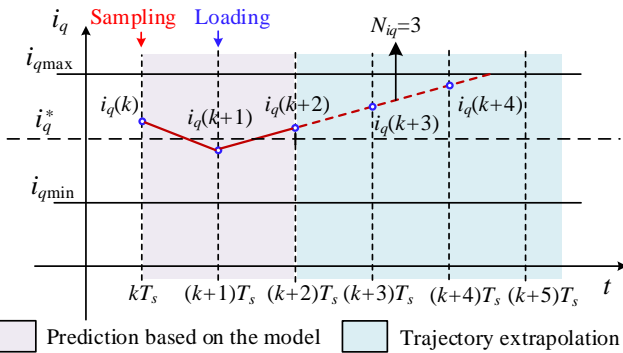


Fig. 6. Principle of trajectory extrapolation method [42].

The MPC for DTP-PMSM can be established based on two separate three-phase inverters. Conventionally, the sampling and control of the two sets of three-phase windings are implemented synchronously. However, the DTP-PMSM drives provide additional control freedom to improve the control performance. The sampling and control algorithm of the two sets of three-phase windings can be executed alternatively, such that the equivalent sampling and control frequency of the drive is doubled [52]. Fig. 7 compares the control sequences of the synchronous control and the interleaved control. It can be seen that the control delay is reduced by half while the control frequency is doubled, which ensures better control performance. Moreover, the interleaved control avoids the cross-traversal of vector candidate sets between two sets of three-phase windings and the computational complexity can be reduced effectively. Fig. 8 compares the experimental stator current waveforms in phases A, B, D and E using synchronous MPC and interleaved MPC schemes at the 50 Hz fundamental operating condition. It can be observed that the interleaved MPC presents better current harmonic performance even with lower average switching frequency. This is due to the doubled equivalent sampling and control frequency with interleaved MPC.

C. VSD-MPC for DTP-PMSM

Another MPC implementation for DTP-PMSM is based on

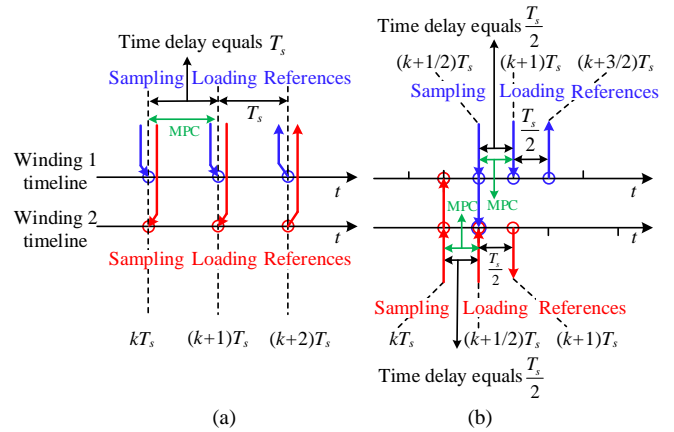


Fig. 7. Comparison of control sequence [52]. (a) Synchronous control. (b) Proposed interleaved control.

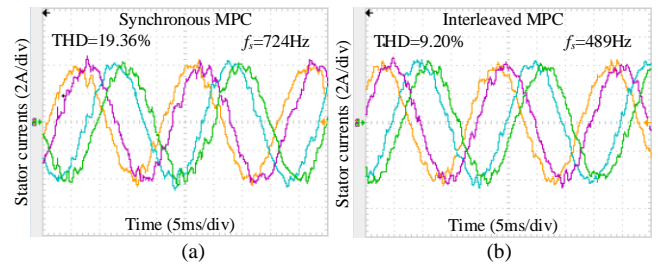


Fig. 8. Stator currents of phases A, B, D, and E [52]. (a) Current waveforms using synchronous MPC. (b) Current waveforms using interleaved MPC.

space vector using VSD. Fig. 9 shows the vector diagram of six-phase two-level inverter using the VSD approach [42]. The switching state is identified by two decimal numbers equivalent to the binary number of two three-phase inverters. For instance, the switching state “110100” for phases A, B, C, D, E, F is identified as “64”. Both the total numbers of voltage vectors in $\alpha\beta$ - and xy - subspaces are 64. The switching state with the largest vector length in the $\alpha\beta$ -subspace corresponds to the smallest vector length in the xy -subspace. Therefore, the 12 largest vectors in $\alpha\beta$ -subspace are selected as candidate vectors for the trajectory extrapolated MPC to achieve the largest voltage-transfer ratio in the $\alpha\beta$ -subspaces. Fig. 10 shows the control diagram of the VSD based trajectory extrapolated MPC scheme [42]. It can be observed that the control scheme can be summarized as two steps: the vector candidate selection and the candidate evaluation based on motor model and cost function.

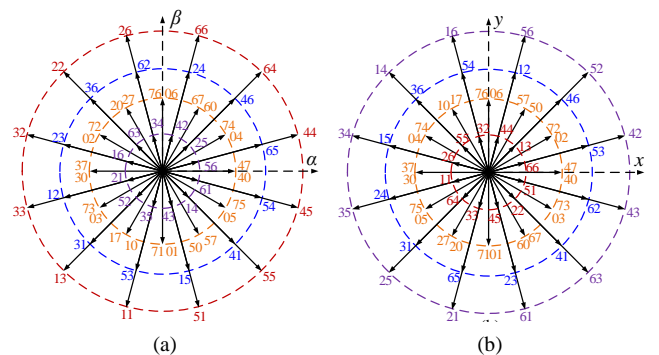


Fig. 9. Six-phase two-level space vector diagram [42]. (a) $\alpha\beta$ -subspace. (b) xy -subspace.

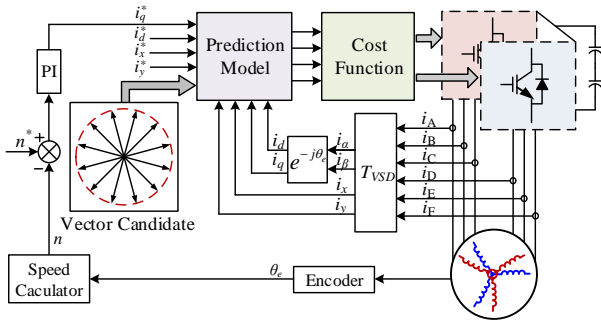


Fig. 10. Control diagram of VSD based trajectory extrapolated MPC [42].

IV. OPTIMIZED PULSE PATTERN BASED CONTROL

A. OPP Based LCR Techniques for Three-phase Motor Drives

The basic idea of the OPP based modulation is to use offline optimized switching sequences for better modulation performance. However, the main limitation of the conventional OPP based control is the poor dynamic performance due to the look-up table method. Hybrid modulation method and flux trajectory control are two main solutions to improve dynamic performance. Hybrid modulation schemes are employed in [34]-[35] where selected harmonic elimination PWM (SHEPWM) is used for steady-state conditions, whereas the modulation switches to SVM at dynamic conditions. Another hybrid modulation method is proposed in [36], where SVM is used for flux trajectory tracking at dynamic conditions and OPP is used at steady-state conditions. The current or flux trajectory control without strategy switching is proposed in [37]-[38], where the switching instants of switching devices are directly manipulated in a deadbeat manner by closed-loop control of stator current or flux trajectory. Further, the model predictive pulse pattern control (MP³C) is proposed based on the flux trajectory tracking in [39]-[41], which has the advantages of long prediction horizon and needs no requirement for separate control of fundamental and harmonic components. The high sampling frequency of MP³C scheme contributes to its fast dynamic performance, which is verified at the same level as DTC [40].

B. Optimized Pulse Pattern Based PWM for DTP-PMSM

As aforementioned, one of the main differences between three-phase PMSM and DTP-PMSM lies in that the impedance of the harmonic subspace is smaller than that of the torque subspace given the magnetic coupling between dual three-phase windings. Moreover, currents in the harmonic subspace generate no torque ripple component for surface-mounted DTP-PMSM with sinusoidal back electromotive force (EMF) [42]. Therefore, the OPP designed for three-phase PMSM is not the optimal solution for DTP-PMSM. Recently, the OPP for DTP-PMSM has been investigated, where both PWM strategy for current THD minimization and for torque ripple minimization are proposed [42], [53]-[55]. Fig. 11 shows a typical waveform of the inverter output voltage in phase A. N denotes the number of switching angles ($\alpha_i, i=1, 2, \dots, N$) within a quarter of the fundamental period. The six-phase stator voltages are expressed as:

$$\begin{bmatrix} u_A \\ u_B \\ u_C \\ u_D \\ u_E \\ u_F \end{bmatrix} = \begin{bmatrix} \sum_{n=1,3,5,\dots}^{\infty} U_n \sin[n(\omega t + \varphi + \pi)] \\ \sum_{n=1,3,5,\dots}^{\infty} U_n \sin[n(\omega t + \varphi + \pi - 2\pi/3)] \\ \sum_{n=1,3,5,\dots}^{\infty} U_n \sin[n(\omega t + \varphi + \pi - 4\pi/3)] \\ \sum_{n=1,3,5,\dots}^{\infty} U_n \sin[n(\omega t + \varphi + \pi - \pi/6)] \\ \sum_{n=1,3,5,\dots}^{\infty} U_n \sin[n(\omega t + \varphi + \pi - 5\pi/6)] \\ \sum_{n=1,3,5,\dots}^{\infty} U_n \sin[n(\omega t + \varphi + \pi - 9\pi/6)] \end{bmatrix} \quad (14)$$

$$U_n = -\frac{2U_{dc}}{n\pi} \left[1 + 2 \sum_{i=1}^N (-1)^i \cos(n\alpha_i) \right] \quad (15)$$

where U_n denotes the amplitude of the voltage in order of n ($n=1, 3, 5, \dots$). φ denotes the torque angle, which is the phase difference between fundamental stator voltage and PM flux linkage in phase A. The VSD transform maps the harmonics in order of $12h-5$ and $12h-7$ to the harmonic subspace, whereas it maps the harmonics in order of $12h+1$ and $12h-1$ to the torque subspace. The amplitudes of these harmonics can be expressed as:

$$U_{12h+1} = -\frac{2U_{dc}}{(12h+1)\pi} \left\{ 1 + 2 \sum_{i=1}^N (-1)^i \cos[(12h+1)\alpha_i] \right\} \quad (16)$$

$$U_{12h-1} = -\frac{2U_{dc}}{(12h-1)\pi} \left\{ 1 + 2 \sum_{i=1}^N (-1)^i \cos[(12h-1)\alpha_i] \right\}$$

$$U_{12h-5} = -\frac{2U_{dc}}{(12h-5)\pi} \left\{ 1 + 2 \sum_{i=1}^N (-1)^i \cos[(12h-5)\alpha_i] \right\} \quad (17)$$

$$U_{12h-7} = -\frac{2U_{dc}}{(12h-7)\pi} \left\{ 1 + 2 \sum_{i=1}^N (-1)^i \cos[(12h-7)\alpha_i] \right\}$$

With the assumption of sinusoidal back EMF, the current harmonics of these orders can be expressed as:

$$I_{12h-1} = \frac{U_{12h-1}}{(12h-1)\omega L_s}, \quad I_{12h+1} = \frac{U_{12h+1}}{(12h+1)\omega L_s} \quad (18)$$

$$I_{12h-5} = \frac{U_{12h-5}}{(12h-5)\omega L_s}, \quad I_{12h-7} = \frac{U_{12h-7}}{(12h-7)\omega L_s} \quad (19)$$

Consequently, the optimization problem can be established as:

$$\begin{aligned} \min_{\alpha_1, \alpha_2, \dots, \alpha_N} i_{\text{harm-rms}} &= \frac{1}{\sqrt{2}} \sqrt{\left(\frac{1}{\omega L_s} \right)^2 \sum_{h=1}^{\infty} \left[\left(\frac{U_{12h+1}}{12h+1} \right)^2 + \left(\frac{U_{12h-1}}{12h-1} \right)^2 \right] +} \\ &\quad \left(\frac{1}{\omega L_s} \right)^2 \sum_{h=1}^{\infty} \left[\left(\frac{U_{12h-5}}{12h-5} \right)^2 + \left(\frac{U_{12h-7}}{12h-7} \right)^2 \right] \quad (20) \\ \text{s.t.} &\quad \begin{cases} - \left[1 + 2 \sum_{i=1}^N (-1)^i \cos(\alpha_i) \right] = m\pi/2 \\ 0 < \alpha_1 < \alpha_2 < \dots < \alpha_N < \pi/2 \end{cases} \end{aligned}$$

The modulation index m is defined as $m=U_1/U_{dc}$. It can be seen that the impedances of different subspaces equivalently perform as the weighting factors for optimization.

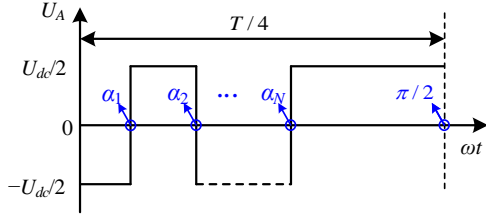


Fig. 11. Typical waveform of inverter output voltage in phase A [42].

On the other hand, the torque ripple can also be optimized for DTP-PMSM. The stator voltage vector in the synchronous rotating frame of the torque subspace can be expressed as:

$$\begin{aligned} \mathbf{u}_{dq} &= e^{j-\omega t} \frac{1}{3} \left(u_A e^{j0} + u_B e^{j\frac{2\pi}{3}} + u_C e^{j\frac{4\pi}{3}} + u_D e^{j\frac{\pi}{6}} + u_E e^{j\frac{5\pi}{6}} + u_F e^{j\frac{7\pi}{6}} \right) \\ &= \sum_{n=12h+1}^{\infty} U_n e^{j[12h\omega t + n\varphi + \frac{\pi}{2}(2n-1)]} + \sum_{n=12h-1}^{\infty} U_n e^{j[-12h\omega t - n\varphi - \frac{\pi}{2}(2n-1)]} \end{aligned} \quad (21)$$

It can be observed in (21) that the voltage harmonics in order of $12h+1$ synthesize voltage vectors with angular frequency of $12h\omega$ in positive sequence, whereas those in order of $12h-1$ synthesize voltage vectors with angular frequency of $12h\omega$ in negative sequence. Consequently, the final synthetic trajectories of the voltage vectors are a cluster of ellipses. Fig. 12 shows the example of vector trajectory with angular frequency of 12ω [53]. The phase angle of the major and minor axes of the ellipse trajectory can be expressed as:

$$\begin{cases} \theta_{L12h} = \varphi + \frac{1}{4}\pi - \frac{\pi}{4} \text{sgn}(U_{12h-1}U_{12h+1}) + l\pi, l \in \mathbf{Z} \\ \theta_{S12h} = \varphi - \frac{1}{4}\pi - \frac{\pi}{4} \text{sgn}(U_{12h-1}U_{12h+1}) + l\pi, l \in \mathbf{Z} \end{cases} \quad (22)$$

where l is an integer, and $\text{sgn}(\cdot)$ represents the sign function. Further, the current harmonic vector can be calculated as:

$$\mathbf{i}_{dq} = \sum_{n=12h+1}^{\infty} I_n e^{j[12h\omega t + n\varphi + \frac{\pi}{2}(2n-2)]} + \sum_{n=12h-1}^{\infty} I_n e^{j[-12h\omega t - n\varphi - \frac{\pi}{2}(2n-2)]} \quad (23)$$

where I_n denotes the amplitude of the current harmonic in order of n . The phase angles of the major and the minor axes of the current vector trajectory are the same as those of the voltage vector trajectory, respectively. The length of the major $i_{\Sigma 12h}$ and the minor radius $i_{\Delta 12h}$ of the ellipse current trajectory can be calculated as:

$$\begin{cases} i_{\Sigma 12h} = \frac{U_{12h-1}}{(12h-1)\omega L_s} + \frac{U_{12h+1}}{(12h+1)\omega L_s} \\ i_{\Delta 12h} = \frac{U_{12h-1}}{(12h-1)\omega L_s} - \frac{U_{12h+1}}{(12h+1)\omega L_s} \end{cases} \quad (24)$$

Therefore, the amplitude of 12th torque ripple T_{e12} can be expressed in (25), and the final RMS value of the total torque ripple is given in (26), where N_p denotes the pole pair number:

$$|T_{e12}| = 3N_p \psi_f \sqrt{(\sin \theta_{L12})^2 i_{\Sigma 12}^2 + (\cos \theta_{L12})^2 i_{\Delta 12}^2} \quad (25)$$

$$T_{e-\text{rms}} = \frac{3N_p \psi_f}{\sqrt{2}} \sqrt{\sum_{k=1}^{\infty} \left[(\sin \theta_{L12k})^2 i_{\Sigma 12k}^2 + (\cos \theta_{L12k})^2 i_{\Delta 12k}^2 \right]} \quad (26)$$

Consequently, the optimization problem for comprehensive current and torque ripple mitigation can be established as:

$$\begin{aligned} \min J &= \lambda_T \frac{T_{e-\text{rms}}}{3N_p \psi_f} + (1 - \lambda_T) i_{\text{harm-rms}} \\ \text{s.t.} &\begin{cases} -\left[1 + 2 \sum_{i=1}^N (-1)^i \cos(\alpha_i) \right] = m\pi / 2 \\ 0 \leq \alpha_1 \leq \alpha_2 \leq \dots \leq \alpha_N \leq \pi / 2 \end{cases} \end{aligned} \quad (27)$$

where λ_T is a weighting factor.

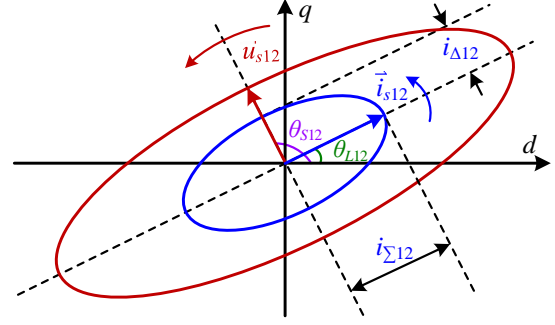
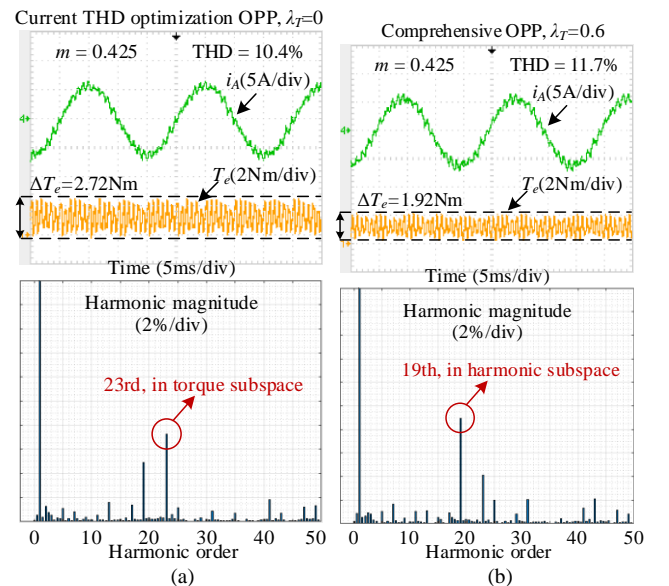


Fig. 12. Synthetic trajectory of 11th and 13th order currents and voltages in the dq-frame [53].

Fig. 13 compares the control performance of the two kinds of OPPs [53]. The OPP in Fig. 13(a) is designed for current THD minimization ($\lambda_T=0$), whereas that in Fig. 13(b) is designed for comprehensive mitigation of current and torque harmonics ($\lambda_T=0.6$). The switching frequency is 750 Hz and the carrier ratio is 15. It can be observed that the torque ripple of DTP-PMSM in Fig. 13(b) is decreased by 29.4% from 2.72 N m to 1.92 N m with the modulation index m equaling 0.425. On the other hand, the current THD is slightly increased from 10.4% to 11.7%. Therefore, it is verified that the current and torque harmonic performance can be optimized comprehensively for DTP-PMSM drives using OPP based modulation schemes.


 Fig. 13. Current and torque waveforms along with current spectrums in experiments [53]. (a) Current THD OPP with m equaling 0.425. (b) Comprehensive OPP with m equaling 0.425.

C. MP^3C for DTP-PMSM

Fig. 14 shows the control diagram of MP^3C for DTP-PMSM [42]. The flux reference is calculated using the voltage model based on the offline optimized switching sequence described in Section IV-B or any other type of OPP modulation. The stator flux linkage is estimated online and is controlled to track the reference flux linkage trajectory by directly modifying the switching instants of switching devices. The flux reference vector ψ_{VSD}^* can be calculated using voltage based flux model as:

$$\psi_{VSD}^*(t) = \frac{U_{dc}}{2} \int_0^t T_{VSD} u_{sgn}(\tau) d\tau - \frac{U_{dc}}{2T_f} \int_0^{T_f} \int_0^t T_{VSD} u_{sgn}(\tau) d\tau dt \quad (28)$$

where U_{dc} is the DC-link voltage. T_f is the fundamental period, and u_{sgn} is the symbolic function corresponding to the switching states S_x ($x \in \{a, b, c, d, e, f\}$) in each phase as:

$$\begin{aligned} u_{sgn} &= [u_a, u_b, u_c, u_d, u_e, u_f]^T \\ u_x &= \begin{cases} 1, & S_x = 1 \\ -1, & S_x = 0 \end{cases}, \quad x \in \{a, b, c, d, e, f\}. \end{aligned} \quad (29)$$

It can be seen that the flux reference is directly determined by the selected pulse pattern. Then, the actual stator flux ψ_{VSD} can be obtained with current or voltage based flux model, and the flux linkage tracking error can be calculated as:

$$\psi_{error} = \psi_{VSD}^* - \psi_{VSD} \quad (30)$$

Fig. 15 shows the principle of the pulse pattern control method in phase A [42]. The sampling is implemented at instant t_0 . The sampling period is T_s and the prediction horizon is T_p . The switching instant in black lines corresponds to the initial optimal switching sequence. There are four switching actions within the prediction horizon located at instants t_1 , t_2 , t_3 and t_4 , respectively. Then, the switching instants are modified as the red dashed lines in Fig. 15. Accordingly, the variation in the stator flux of phase A $\Delta\psi_A$ against the initial switching angles can be calculated as:

$$\Delta\psi_A = U_{dc} (\Delta t_1 + \Delta t_2 + \Delta t_3 + \Delta t_4) \quad (31)$$

where Δt_1 , Δt_2 , Δt_3 and Δt_4 are the variation in switching instants. It can be observed that the stator flux linkage in phase A can be regulated by modifying the switching instants directly.

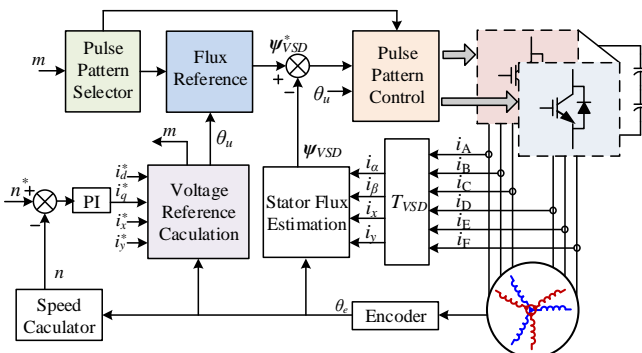


Fig. 14. Control diagram of MP^3C for DTP-PMSM [42].

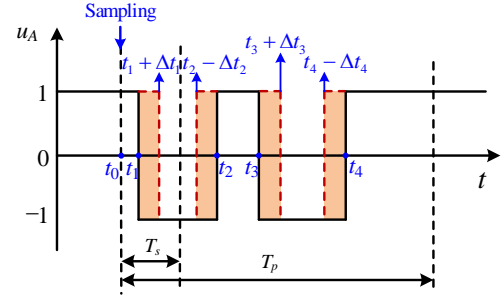


Fig. 15. Principle of the pulse pattern control method [42].

To determine the shifts of switching instant in each phase for flux linkage trajectory tracking, the cost function $J(\Delta t)$ is established as:

$$\begin{aligned} \min_{\Delta t} J(\Delta t) &= \min_{\Delta t} \left[\|\psi_{error} - \psi_{corr}(\Delta t)\|^2 + q \Delta t^T \Delta t \right] \\ \text{s.t. } kT_s &\leq t_{x1} \leq t_{x2} \leq \dots \leq t_{xn_x} \leq t_{x(n_x+1)}^*, x \in \{a, b, c, d, e, f\} \end{aligned} \quad (32)$$

where ψ_{corr} is the variation of stator flux linkage due to the shift of switching instant, Δt is the vector composed of switching instant shift values in all phases, and q is the weighting factor to limit the changes on the initial optimal switching sequence. The restrictive condition of $J(\Delta t)$ is that the shifted switching instants follow the time sequence. The optimization problem shown in (32) can be solved online by using active set method as in [42].

Fig. 16 presents experimental results of dynamic response using the conventional look-up table method and MP^3C for DTP-PMSM where SHEPWM is exemplified for comparison. The load torque suddenly switches from 0.25p.u. to 1.0p.u. at 1000 rpm (50 Hz) operating condition. As shown in Fig. 16, it takes around 540 ms for SHEPWM using conventional look-up table method to return to steady-state operation, which lasts longer than the duration of 220 ms required by the MP^3C scheme. Therefore, it is verified that the MP^3C scheme can effectively improve the dynamic control performance for DTP-PMSM drives using OPP based control schemes. The variation in speed during the transient process of MP^3C scheme is also smaller than that of the look-up table method. Moreover, the steady-state torque ripple using MP^3C scheme is smaller than that using the look-up table method. The reason is that the flux trajectory tracking control employed in the inner loop in the MP^3C scheme can effectively mitigate the persistent perturbation caused by speed control loop at steady state.

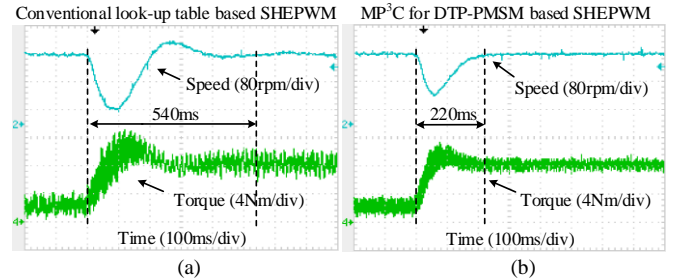


Fig. 16. Dynamic performance comparison of SHEPWM using different control methods. (a) Conventional look-up table method. (b) MP^3C for DTP-PMSM.

V. COMPARISON AND DISCUSSION

A. Performance Comparison

Table I presents comparison of the aforementioned three categories of control methods for DTP-PMSM drives with low carrier ratios. Method 1 denotes MS-SVM based complex vector control. Method 2 denotes the trajectory extrapolated MPC. Method 3 denotes the OPP based MP³C scheme. For the dual three-phase windings with magnetic coupling, the low impedance of harmonic subspace causes significant degradation of current harmonic performance for SVM based modulation methods. On the other hand, the trajectory extrapolated MPC methods possess better harmonic performance due to the online optimization of voltage vector selection. Furthermore, the OPP based MP³C scheme presents the best harmonic performance since offline optimization of harmonics is implemented. Moreover, it is found that dynamic control performance of the three categories of methods is almost at the same level since high sampling frequencies are employed in all three schemes. Additionally, the overall computational complexity of the compared methods is close when considering the difference in sampling frequency [42].

For dual three-phase windings with weak magnetic coupling, the comparison between OPP with λ_T equaling 0 and OPP with λ_T equaling 0.8 is presented in Fig. 17 [53]. By employing λ_T to be 0.8, the torque ripple of DTP-PMSM can be reduced from 3.84 N m to 1.44 N m at $m=0.35$ and from 2.72 N m to 1.04 N m at $m=0.425$. Therefore, it is verified that the trade-off design of performance in torque ripple and current harmonics can be achieved by distributing the current components in the torque subspace and harmonic subspace of DTP-PMSM. On the other hand, CPS-SVM can be regarded as a suboptimal case of OPP because the basic SVPWM switching sequence is still used in each three-phase inverter. Therefore, the current and torque ripple performance using OPP could be better than that using CPS-SVM theoretically. However, it should be noted that the advantage of CPS-SVM is the relatively simple implementation.

TABLE I
COMPARISON OF DIFFERENT MODULATION AND CONTROL SCHEMES

Methods	Method 1	Method 2	Method 3
Current THD	Medium	Good	Best
Torque ripple	Good	Good	Best
Dynamic response	Fast	Fast	Fast

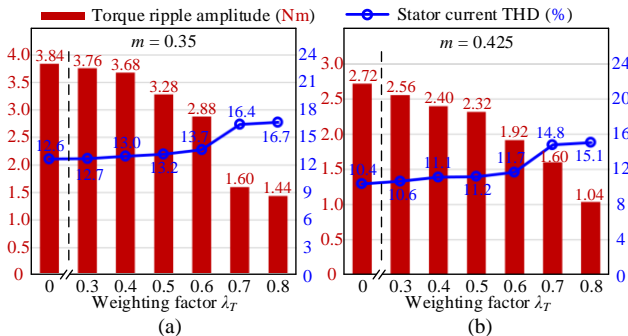


Fig. 17. Comparison of current THD and torque ripple with different values of weighting factor λ_T [53]. (a) $m=0.35$. (b) $m=0.425$.

B. Discussion of Future Trends

Considering that the magnetic coupling of DTP-PMSM influences the performance of current harmonic suppression, the DTP-PMSM is considered for those with and without magnetic coupling separately. For DTP-PMSM with two sets of three-phase windings coupled magnetically, the main challenge of the LCR operation is the mitigation of low-order harmonics due to the small inductance characteristic in the harmonic subspace. The OPP based MP³C scheme is an effective solution, which could approach the best harmonic performance theoretically and maintain fast dynamic performance simultaneously. Therefore, the trend is that the OPP based MP³C scheme is more suitable for LCR operation of DTP-PMSM drives where there exists distinct magnetic coupling between dual three-phase windings. The stability analysis and state observation are to be further investigated for the OPP based MP³C schemes to increase robustness against disturbance in wide operation domains. It should be mentioned that from the perspective of improving the robustness, there are some other control methods such as model-free MPC, data-driven MPC and disturbance observation based composite control schemes. Their applications require further investigation to address the difference and difficulties of LCR based DTP-PMSM drives compared to their three-phase counterparts.

On the other hand, the impedance characteristic for DTP-PMSM without coupling between dual three-phase windings is similar to three-phase PMSM. The main advantage of DTP-PMSM over three-phase PMSM lies in that components in the harmonic subspace of DTP-PMSM generate no torque ripple, while they provide additional freedoms for optimal operation of drives. CPS-SVM is convenient to be implemented for improving performance of DTP-PMSM without coupling between dual three-phase windings. A universal phase-shift angle can be investigated for comprehensive optimization with different objectives. Additionally, the stator inductance of high-speed machines is usually very small, which could cause large stator current harmonics when using SVPWM modulation. In that case, the OPP based MP³C scheme is recommended with comprehensive mitigation of current harmonics and torque ripples for DTP-PMSM drives.

VI. CONCLUSION

This paper presents a technical review of recent work on LCR modulation strategies and control schemes of DTP-PMSM drives. Compared to the LCR control for three-phase PMSM drives, the main challenge of LCR control for DTP-PMSM is to suppress the distinct low-order current harmonics in the harmonic subspace, which is caused by the small inductance characteristic of DTP-PMSM with magnetic coupling between dual three-phase windings. The MS-SVM based complex vector control and the CPS-SVM can help reduce control delay, low-order harmonics and torque ripple of DTP-PMSM with low carrier ratios. But they still suffer from the inherent harmonics caused by SVM. By sampling and executing algorithm of trajectory extrapolated MPC in an

interleaved sequence, the current harmonics and the torque ripples can be reduced for DTP-PMSM drives with low carrier ratios. This method is convenient and efficient for DTP-PMSM drives with magnetically decoupled dual-three-phase windings. However, its performance will be deteriorated for drives with low inductances, e.g., the dual three-phase windings with strong magnetic coupling and high-speed drives. The OPP based methods present the best steady-state performance for LCR DTP-PMSM in current harmonics and torque ripples by optimization offline. Among them, MP³C can further improve the DTP-PMSM drives' dynamics by adjusting the pulse pattern to track the optimal flux trajectory.

REFERENCES

- [1] X. Q. Wang, Z. Wang, and Z. X. Xu, "A Hybrid Direct Torque Control Scheme for Dual Three-phase PMSM Drives with Improved Operation Performance," *IEEE Trans. on Power Electron.*, vol. 34, no. 2, pp. 1622–1634, Feb. 2019.
- [2] X. Q. Wang, Z. Wang, and Z. X. Xu *et al.*, "Comprehensive Diagnosis and Tolerance Strategies for Electrical Faults and Sensor Faults in Dual Three-phase PMSM Drives," *IEEE Trans. on Power Electron.*, vol. 34, no. 7, pp. 6669–6684, Jul. 2019.
- [3] A. Edpuganti, and A. K. Rathore, "A Survey of Low Switching Frequency Modulation Techniques for Medium-voltage Multilevel Converters," *IEEE Trans. on Ind. Appl.*, vol. 51, no. 5, pp. 4212–4228, Sept.-Oct. 2015.
- [4] P. C. Liu, Z. Wang, and S. M. Wei *et al.*, "Recent Developments of Modulation and Control for High-power Current-source-converters Fed Electric Machine Systems," *CES Trans. on Elect. Mach. and Syst.*, vol. 4, no. 3, pp. 215–226, Sept. 2020.
- [5] J. X. Shen, X. F. Qin, and Y. C. Wang, "High-speed Permanent Magnet Electrical Machines—applications, Key Issues and Challenges," *CES Trans. on Elect. Mach. and Syst.*, vol. 2, no. 1, pp. 23–33, Mar. 2018.
- [6] A. El-Refaie, and M. Osama, "High Specific Power Electrical Machines: a System Perspective," *CES Trans. on Elect. Mach. and Syst.*, vol. 3, no. 1, pp. 88–93, Mar. 2019.
- [7] W. J. Zhang, Z. H. Song, and W. X. Yao *et al.*, "Single Active Vector Pulsewidth Modulation with Improved Harmonic and Dynamic Performance for Low-carrier Ratio Applications," *IEEE Trans. on Power Electron.*, vol. 39, no. 5, pp. 5649–5661, May 2024.
- [8] L. Yang, Z. Q. Zhu, and H. Bin *et al.*, "Spectral Analysis and Sideband Harmonic Cancellation of Six-step Operation with Low Carrier-fundamental Frequency Ratio for High-speed Brushless DC Drives," *IEEE Trans. on Ind. Electron.*, vol. 68, no. 9, pp. 7778–7792, Sept. 2021.
- [9] G. R. Walker, "Digitally-implemented Naturally Sampled PWM Suitable for Multilevel Converter Control," *IEEE Trans. on Power Electron.*, vol. 18, no. 6, pp. 1322–1329, Nov. 2003.
- [10] J. Y. Dai, Y. Q. Lang, and B. Wu *et al.*, "A Multisampling SVM Scheme for Current Source Converters with Superior Harmonic Performance," *IEEE Trans. on Power Electron.*, vol. 24, no. 11, pp. 2436–2445, Nov. 2009.
- [11] S. He, D. Zhou, and X. F. Wang *et al.*, "A Review of Multisampling Techniques in Power Electronics Applications," *IEEE Trans. on Power Electron.*, vol. 37, no. 9, pp. 10514–10533, Sept. 2022.
- [12] S. He, D. Zhou, and X. F. Wang *et al.*, "Aliasing Suppression of Multisampled Current-controlled LCL-filtered Inverters," *IEEE J. of Emerg. and Sel. Topics in Power Electron.*, vol. 10, no. 2, pp. 2411–2423, Apr. 2022.
- [13] Q. Wei, B. Wu, and D. W. Xu *et al.*, "A Natural-sampling-based SVM Scheme for Current Source Converter with Superior Low-order Harmonics Performance," *IEEE Trans. on Power Electron.*, vol. 31, no. 9, pp. 6144–6154, Sept. 2016.
- [14] Q. Wei, B. Wu, and D. D. Xu *et al.*, "Optimal Space Vector Sequence Investigation based on Natural Sampling SVM for Medium-voltage Current-source Converter," *IEEE Trans. on Power Electron.*, vol. 32, no. 1, pp. 176–185, Jan. 2017.
- [15] P. C. Liu, Z. Wang, and Y. Xu *et al.*, "Improved Harmonic Profile for High-power PWM Current-source Converters with Modified Space-vector Modulation Schemes," *IEEE Trans. on Power Electron.*, vol. 36, no. 10, pp. 11234–11244, Oct. 2021.
- [16] J. Holtz, J. T. Quan, and J. Pontt *et al.*, "Design of Fast and Robust Current Regulators for High-power Drives based on Complex State Variables," *IEEE Trans. on Ind. Appl.*, vol. 40, no. 5, pp. 1388–1397, Sept.-Oct. 2004.
- [17] J. Holtz, and N. Oikonomou, "Fast Dynamic Control of Medium Voltage Drives Operating at Very Low Switching Frequency—an Overview," *IEEE Trans. on Ind. Electron.*, vol. 55, no. 3, pp. 1005–1013, Mar. 2008.
- [18] J. S. Yim, S. K. Sul, and B. H. Bae *et al.*, "Modified Current Control Schemes for High-performance Permanent-magnet AC Drives with Low Sampling to Operating Frequency Ratio," *IEEE Trans. on Ind. Appl.*, vol. 45, no. 2, pp. 763–771, Mar.-Apr. 2009.
- [19] A. M. Diab, S. S. Yeoh, and S. Bozhko *et al.*, "Enhanced Active Disturbance Rejection Current Controller for Permanent Magnet Synchronous Machines Operated at Low Sampling Time Ratio," *IEEE J. of Emerg. and Sel. Topics in Ind. Electron.*, vol. 3, no. 2, pp. 230–241, Apr. 2022.
- [20] Y. Liang, D. L. Liang, and S. F. Jia *et al.*, "Digital Current Controller Design for SPMSM with Low Switching-to-fundamental Frequency Ratios," *IEEE Trans. on Ind. Appl.*, vol. 58, no. 4, pp. 4685–4697, Jul.-Aug. 2022.
- [21] J. D. Zhang, F. Peng, and Y. K. Huang *et al.*, "Discrete-time-model-based Dynamic Decoupling Active Damping Current Control for CSI-fed High-speed PMSM with Low Carrier Ratio," *IEEE Trans. on Power Electron.*, vol. 39, no. 6, pp. 6783–6802, Jun. 2024.
- [22] A. Sheianov, X. Xiao, and X. D. Sun, "An Enhanced Current Control Structure for Ultra-high-speed Permanent Magnet Synchronous Motor Applications," *IEEE Trans. on Ind. Appl.*, vol. 60, no. 3, pp. 4987–5001, May-Jun. 2024.
- [23] H. Kim, M. W. Degner, and J. M. Guerrero *et al.*, "Discrete-time Current Regulator Design for AC Machine Drives," *IEEE Trans. on Ind. Appl.*, vol. 46, no. 4, pp. 1425–1435, Jul.-Aug. 2010.
- [24] S. J. Dai, J. B. Wang, and Z. G. Sun *et al.*, "Deadbeat Predictive Current Control for High-speed Permanent Magnet Synchronous Machine Drives with Low Switching-to-fundamental Frequency Ratios," *IEEE Trans. on Ind. Electron.*, vol. 69, no. 5, pp. 4510–4521, May 2022.
- [25] G. J. Pei, J. X. Liu, and X. N. Gao *et al.*, "Deadbeat Predictive Current Control for SPMSM at Low Switching Frequency with Moving Horizon Estimator," *IEEE J. of Emerg. and Sel. Topics in Power Electron.*, vol. 9, no. 1, pp. 345–353, Feb. 2021.
- [26] S. J. Dai, J. B. Wang, and Z. G. Sun *et al.*, "Model Inaccuracy Analysis and Compensation of Stationary Frame-based Deadbeat Predictive Current Control for High-speed PMSM Drives," *IEEE Trans. on Transp. Electrific.*, vol. 8, no. 2, pp. 2654–2666, Jun. 2022.
- [27] T. Geyer, "Generalized Model Predictive Direct Torque Control: Long Prediction Horizons and Minimization of Switching Losses," in *Proc. of 48th IEEE Conf. on Decision and Control held jointly with 2009 28th Chin. Control Conf.*, Shanghai, China, Dec. 2009, pp. 6799–6804.
- [28] T. Geyer, G. Papafotiou, and M. Morari, "Model Predictive Direct Torque Control—part I: Concept, Algorithm, and Analysis," *IEEE Trans. on Ind. Electron.*, vol. 56, no. 6, pp. 1894–1905, Jun. 2009.
- [29] T. Geyer, "Model Predictive Direct Current Control: Formulation of the Stator Current Bounds and the Concept of the Switching Horizon," *IEEE Ind. Appl. Mag.*, vol. 18, no. 2, pp. 47–59, Mar.-Apr. 2012.
- [30] P. Karamanakos, T. Geyer, and R. Kennel, "A Computationally Efficient Model Predictive Control Strategy for Linear Systems with Integer Inputs," *IEEE Trans. on Control Syst. Technol.*, vol. 24, no. 4, pp. 1463–1471, Jul. 2016.
- [31] T. Dorfling, H. du Toit Mouton, and T. Geyer *et al.*, "Long-horizon Finite-control-set Model Predictive Control with Nonrecursive Sphere Decoding on an FPGA," *IEEE Trans. on Power Electron.*, vol. 35, no. 7, pp. 7520–7531, Jul. 2020.
- [32] P. Karamanakos, T. Geyer, and R. P. Aguilera, "Long-horizon Direct Model Predictive Control: Modified Sphere Decoding for Transient

- Operation," *IEEE Trans. on Ind. Appl.*, vol. 54, no. 6, pp. 6060–6070, Nov.-Dec. 2018.
- [33] T. Geyer, and D. E. Quevedo, "Multistep Finite Control Set Model Predictive Control for Power Electronics," *IEEE Trans. on Power Electron.*, vol. 29, no. 12, pp. 6836–6846, Dec. 2014.
- [34] Z. Wang, B. Wu, and D. W. Xu *et al.*, "Hybrid PWM for High-power Current-source-inverter-fed Drives with Low Switching Frequency," *IEEE Trans. on Power Electron.*, vol. 26, no. 6, pp. 1754–1764, Jun. 2011.
- [35] Z. Wang, B. Wu, and D. W. Xu *et al.*, "A Current-source-converter-based High-power High-speed PMSM Drive with 420-Hz Switching Frequency," *IEEE Trans. on Ind. Electron.*, vol. 59, no. 7, pp. 2970–2981, Jul. 2012.
- [36] S. J. Dai, J. B. Wang, and Z. G. Sun *et al.*, "Mode Transition of Synchronous Optimal Modulation for High-speed PMSM Drives," *IEEE Trans. on Ind. Appl.*, vol. 58, no. 2, pp. 2001–2012, Mar.-Apr. 2022.
- [37] J. Holtz, and B. Beyer, "Fast Current Trajectory Tracking Control based on Synchronous Optimal Pulsewidth Modulation," *IEEE Trans. on Ind. Appl.*, vol. 31, no. 5, pp. 1110–1120, Sept.-Oct. 1995.
- [38] J. Holtz, and N. Oikonomou, "Synchronous Optimal Pulsewidth Modulation and Stator Flux Trajectory Control for Medium-voltage Drives," *IEEE Trans. on Ind. Appl.*, vol. 43, no. 2, pp. 600–608, Mar.-Apr. 2007.
- [39] T. Geyer, N. Oikonomou, and G. Papafotiou *et al.*, "Model Predictive Pulse Pattern Control," *IEEE Trans. on Ind. Appl.*, vol. 48, no. 2, pp. 663–676, Mar.-Apr. 2012.
- [40] T. Geyer, and N. Oikonomou, "Model Predictive Pulse Pattern Control with Very Fast Transient Responses," in *Proc. of 2014 IEEE Energy Convers. Congr. and Expo.*, Pittsburgh, PA, USA, Sept. 2014, pp. 5518–5524.
- [41] T. Geyer, V. Spudić, and W. van der Merwe *et al.*, "Model Predictive Pulse Pattern Control of Medium-voltage Neutral-point-clamped Inverter Drives," in *Proc. of 2018 IEEE Energy Convers. Congr. and Expo.*, Portland, OR, USA, Sept. 2018, pp. 5047–5054.
- [42] M. R. Gu, Z. Wang, and P. C. Liu *et al.*, "Comparative Study of Advanced Modulation and Control Schemes for Dual Three-phase PMSM Drives with Low Switching Frequencies," *IEEE Trans. on Transp. Electrific.*, vol. 10, no. 1, pp. 962–975, Mar. 2024.
- [43] Z. Wang, K. L. Yu, and Y. Q. Li *et al.*, "Position Sensorless Control of Dual Three-phase IPMSM Drives with High-frequency Square-wave Voltage Injection," *IEEE Trans. on Ind. Electron.*, vol. 70, no. 10, pp. 9925–9934, Oct. 2023.
- [44] B. Y. Zheng, J. B. Zou, and Y. X. Xu *et al.*, "High-frequency Current Harmonic Analysis and Suppression in Dual Three-phase PMSMs with Advanced Carrier Phase-shift PWM," *IEEE Trans. on Power Electron.*, vol. 39, no. 2, pp. 2569–2581, Feb. 2024.
- [45] X. C. Wang, H. Yan, and G. Sala *et al.*, "Selective Torque Harmonic Elimination for Dual Three-phase PMSMs based on PWM Carrier Phase Shift," *IEEE Trans. on Power Electron.*, vol. 35, no. 12, pp. 13255–13269, Dec. 2020.
- [46] X. C. Wang, G. Sala, and H. Zhang *et al.*, "Torque Ripple Reduction in Secteded Multi Three-phase Machines based on PWM Carrier Phase Shift," *IEEE Trans. on Ind. Electron.*, vol. 67, no. 6, pp. 4315–4325, Jun. 2020.
- [47] X. Han, D. Jiang, and T. J. Zou *et al.*, "Two-segment Three-phase PMSM Drive with Carrier Phase-shift PWM for Torque Ripple and Vibration Reduction," *IEEE Trans. on Power Electron.*, vol. 34, no. 1, pp. 588–599, Jan. 2019.
- [48] S. Bhattacharya, D. Mascarella, and G. Joć *et al.*, "A Dual Three-level T-NPC Inverter for High-power Traction Applications," *IEEE J. of Emerg. and Sel. Topics in Power Electron.*, vol. 4, no. 2, pp. 668–678, Jun. 2016.
- [49] G. J. Su, and L. X. Tang, "A Segmented Traction Drive System with a Small DC Bus Capacitor," in *Proc. of 2012 IEEE Energy Convers. Congr. and Expo.*, Raleigh, NC, USA, Sept. 2012, pp. 2847–2853.
- [50] Z. Wang, X. Q. Wang, and X. J. Yang *et al.*, "Mitigation of DC-link Current Ripple for Dual Three-phase Flux-adjustable Hybrid PMAC Drives Using Collaborative Switching Strategy," *IEEE Trans. on Ind. Electron.*, vol. 67, no. 9, pp. 7202–7216, Sept. 2020.
- [51] M. R. Gu, Z. Wang, and O. Dordevic, "Analysis and Reduction of Current and Voltage Ripple in DC Link for Three-level NPC Interleaved Dual Three-phase Motor Drives," *IEEE Trans. on Power Electron.*, vol. 38, no. 4, pp. 5128–5140, Apr. 2023.
- [52] M. R. Gu, Z. Wang, and K. L. Yu *et al.*, "Interleaved Model Predictive Control for Three-level Neutral-point-clamped Dual Three-phase PMSM Drives with Low Switching Frequencies," *IEEE Trans. on Power Electron.*, vol. 36, no. 10, pp. 11618–11630, Oct. 2021.
- [53] M. R. Gu, Z. Wang, and B. Wang, "Optimization of Torque Ripple for Low-carrier-ratio Dual Three-phase PMSM with Pulse Pattern Control," *IEEE Trans. on Power Electron.*, vol. 38, no. 12, pp. 15091–15096, Dec. 2023.
- [54] G. Liang, W. Liao, and Z. Y. Zhang *et al.*, "An Optimized Pulsewidth Modulation for Dual Three-phase PMSM Under Low Carrier Ratio," *IEEE Trans. on Power Electron.*, vol. 37, no. 3, pp. 3062–3072, Mar. 2022.
- [55] G. Liang, S. Huang, and W. Liao *et al.*, "An Optimized Modulation of Torque and Current Harmonics Suppression for Dual Three-phase PMSM," *IEEE Trans. on Transp. Electrific.*, vol. 10, no. 2, pp. 3443–3454, Jun. 2024.



Minrui Gu (S'20) received the B.S. degree in electrical engineering from Nanjing University of Science and Technology, Nanjing, China, in 2019, and the M.S. degree in electric engineering from Southeast University, Nanjing, China, in 2021, where he is currently working toward the Ph.D. degree in electrical engineering.

His research interests include control of permanent magnet synchronous motors and modulation of multilevel converters.



Zheng Wang (S'05-M'09-SM'14) received the B.Eng. and M.Eng. degrees from Southeast University, Nanjing, China, in 2000 and 2003, respectively, and the Ph.D. degree from The University of Hong Kong, Hong Kong, in 2008.

From 2008 to 2009, he was a Postdoctoral Fellow in Ryerson University, Toronto, ON, Canada. He is currently a full Professor in the School of Electrical Engineering, Southeast University, China. His research interests include electric drives, power electronics, and renewable power generation. In these fields, he has authored over 120 internationally refereed papers, 1 English book by IEEE-Wiley Press, and 2 English book chapters.

Prof. Wang received IEEE PES Chapter Outstanding Engineer Award and Outstanding Young Scholar Award of Jiangsu Natural Science Foundation of China. He is serving as the Asia Liaison of Transportation System Committee for IEEE IAS, the Vice Chairman of Technical Committee of Renewable Energy System for IEEE IES and an associate editor of IEEE Transactions on Industrial Electronics. He is an IET Fellow and an IEEE VTS Distinguished Lecturer.



Ming Cheng (M'01-SM'02-F'15) received the B.S. and M.S. degrees from the Department of Electrical Engineering, Southeast University, Nanjing, China, in 1982 and 1987, respectively, and the Ph.D. degree from the Department of Electrical and Electronic Engineering, The University of Hong Kong, Hong

Kong, in 2001.

Since 1987, he has been with Southeast University, where he is currently a Professor at the School of Electrical Engineering and the Director of the Research Center for Wind Power Generation. From January to April 2011, he was a Visiting Professor with the Wisconsin Electric Machine and Power Electronics Consortium, University of Wisconsin, Madison. He has authored or co-authored more than 300 technical papers and four books and is the holder of 55 patents in these areas. His teaching and research interests include electrical machines, motor drives for electric vehicles, and renewable energy generation.

Prof. Cheng is a Fellow of the Institution of Engineering and Technology. He has served as the Chair and an Organizing Committee Member for many international conferences. He is a Distinguished Lecturer of the IEEE Industry Applications Society for 2015/2016.



Weifeng Su (Member, IEEE) received the B.Eng. and Ph.D. degrees in electrical engineering from Tsinghua University, Beijing, China, in 1999 and 2004, respectively.

Since Jan 2019, he has worked in China TX IIOT Corporation Limited., and currently serves as the chief scientist. His research interests include system design and advanced control of high-power converters and AC drives in mining, oil&gas and flywheel energy storage applications.



Linyue Shang was born in Yongji, Shanxi, China. He received B.Eng. degree in computer science and technology from Nanjing University of Aeronautics and Astronautics, Nanjing, China.

He is currently a senior engineer with CRRC Xi'an Yonge Electric Intelligent Drive Co., Ltd. His research interests include design, development and debugging of PMSM control systems.



Po Liu was born in Xinzhou, Shanxi, China, in 1979. He received B.Eng. degree in industrial automation from Taiyuan University of Science and Technology, Taiyuan, China, in 2002.

He is currently a professorate senior engineer with CRRC Yongji Electric Co., Ltd., Yongji, China. His research interests include the development of high-voltage high-power induction motors, PMSMs and their control systems.